Laser and Particle Beams (2017), *35*, 210–225.

doi:10.1017/S026303461700009X

Laser generated Richtmyer–Meshkov and Rayleigh–Taylor instabilities and nonlinear wave-vortex paradigm in turbulent mixing. II. Near-central region of Gaussian spot

STJEPAN LUGOMER*

Rudjer Boskovic Institute, Center of Excellence for Advanced Materials and Sensing Devices, Bijenicka c. 54, 10000 Zagreb, Croatia

(Received 5 December 2016; Accepted 16 January 2017)

Abstract

Laser-induced three-dimensional (3D) Richtmyer–Meshkov and Rayleigh–Taylor instabilities (RMI and RTI) on metal target in the semi-confined configuration (SCC) show the new paradigm of wave-vortex mixing. The SCC enables extended lifetime of a hot vapor/plasma plume above the target surface and the formation of fast multiple reshocks. This causes – in the central region (CR) of Gaussian-like spot – the evolution of RMI with the spike breakup (Lugomer, 2016*b*), while in the near CR causes the RMI followed by the RTI. The density interface is transformed into the large-scale broken irregular, quasi-periodic web, which comprises the RTI mushroom-shape spikes and the coherent wave-vortex structures such as the line solitons and vortex filaments. The intensity and direction of reshocks change (due to irregularity of the interface) and cause the formation of domains with the weak and the strong reshocks effects. The weak reshocks affect mushroom-shape spikes only slightly, while the strong ones cause their deformation and symmetry break, bubble collapse, and separation of the horizontal flow into vortex ribbons. Interaction of ribbons with spikes and bubbles causes the ribbon pinning, looping, winding, and formation of knotted and tangled structures. The line solitons, vortex filaments, and ribbons tend to organize into complex large-scale structures with the low wave-vortex turbulent mixing. They represent the new paradigm of 3D RMI and RTI in which the transition to the small-scale turbulent mixing does not appear.

Keywords: coherent structures; laser ablation; Rayleigh–Taylor instability; Richtnyer–Meshkov instability; solitary waves; turbulent mixing; vortex filaments; wave-vortex phenomena

1. INTRODUCTION

The evolution of three-dimensional (3D) laser-induced Richtmyer–Meshkov instability (RMI) on a metal surface by using the semi-confined configuration (SCC) of experiment was studied in paper I (Lugomer, 2016*b*). The beam of Gaussian-like power profile causes different structure evolution under shock wave in the central region (CR), the near-central region (NCR), and the near-periphery region (NPR). The SCC enables a long lifetime of the hot vapor/plasma plume above the target surface extending to ~200–300 μs after pulse termination. It also enables formation of the fast multiple reshocks, which establish the ultrasonic oscillatory field of $\nu \sim 7$–8 MHz (Lugomer, 2016*b*). A complex microfluid dynamics that leads to the new wave-vortex paradigm of emerging coherent structures (Zabusky *et al.*, 2005). The evolution of the new wave-vortex structures in turbulent mixing of the RMI after the shock wave and the series of reshocks in the CR was described in paper I (Lugomer, 2016*b*).

In this paper, we describe characteristics of 3D RMI and Rayleigh–Taylor instability (RTI) and of the mixing structures in the NCR. The nanosecond laser pulse causes plasma detonation and the shock wave that impulsively accelerates the vapor plume [light fluid (ρ_L)] *vertically* into the molten metal layer [heavy fluid (ρ_H)], with baroclinic vorticity deposition and the RMI evolution. The initial perturbation of the interface determines the amplitude and the wavelength of growing spikes and bubbles. Regarding the anisotropic flow and growth of spikes and bubbles depends on the *momentum*, **M**, transferred to the fluid parcel and on the fluid density ratio expressed by the Atwood number,

*Address correspondence and reprint requests to: S. Lugomer, Rudjer Boskovic Institute, Center of Excellence for Advanced Materials and Sensing Devices, Bijenicka c. 54, 10000 Zagreb, Croatia. E-mail: lugomer@irb.hr

$A = (\rho_H - \rho_L)_H + \rho_L$. Both these parameters change in the radial direction due to the *lateral vapor/plasma plume expansion* in the background gas (air) along the microchannel of the SCC (Lugomer, 2016*b*).

The expansion causes decrease of the A number from the CR to the NCR [A(CR) > A(NCR)]. In the same time, the *momentum*, **M**, transferred to the fluid parcel also decreases from the CR into the NCR [**M**(CR) > **M**(NCR)] of the spot. (for details see Lugomer, 2016*b* and the Supplement). The dynamics of a fluid parcel is governed by a balance per unit mass of the *rate of momentum gain* $\boldsymbol{M}$ and the rate of momentum loss $\boldsymbol{M}'$ (Abarzhi, 2010; Lugomer, 2016*a*). Decrease of these parameters is responsible that the shock induced structures at the density interface change in the radial direction from the CR to the NCR of circular Gaussian spot. Their characteristics basically depend on the critical points (Poincare) the nodal point, focal point, and the saddle point at the interface (topological manifold). The saddle point at the shocked interface represents the starting configuration for the evolution of the RMI/RTI structures in the *saddle-point plane* (henceforth, the *base-plane*). The 3D flow field connected with the saddle point on the interface determines the topological characteristics of these structures in the CR and the NCR.

In the CR, a 3D turbulent flow field causes the density interface transformation into the large-scale irregular (quasi-periodic) RMI morphology (called "egg carton"or "egg cartoon"), with the spike breakup (Lugomer, 2016*b*). This morphology of the CR was favorably compared with morphology obtained by 3D numerical simulation of the RMI initiated by the fast and strong shock on the interface of two different gasses (Sin'kova *et al*., 2007; Statsenko *et al.*, 2014).

In the NCR, the evolving morphology is different from the CR, because the RMI is followed by the reversal of pressure and density gradients, which generate the RTI (Miles *et al*., 2005; Suponitsky *et al*., 2013, 2014; Lugomer, 2016*b*). The interface perturbations grow into spikes of heavy-fluid into light-fluid and bubbles of light-fluid into heavy-fluid. The density interface of NCR is transformed into the large-scale irregular quasi-periodic morphology – but in contrast to the CR – it comprises the mushroom-shape spikes. Such morphology indicates that that the dynamics in the direction of acceleration differs dramatically from that in the normal plane (e.g., from the anisotropic), and that dynamics in the normal plane can be regular (periodic) or almost regular (quasi-periodic), or disordered (Abarzhi, 2008; Abarzhi, 2016, Private communication).

Regarding the anisotropic flow and growth of spikes and bubbles for the multimode perturbation the bubble amplitude grows in a different way than the spike amplitude. Various nonlinear models of nonlinear dynamics and of the spike and bubble evolution have been proposed (Lazer, 1955; Zhang, 1998; Abarzhi, 2000) which are discussed in the comparative analysis of Abarzhi (2008). For the nonlinear RMI it is usually assumed that empirical models such as drag model (Alon *et al*., 1996; Zhang, 1998) based on the initial perturbation amplitude of modes give a "reliable insight" on the evolution of a multi-mode initial perturbation. However, there is no clear understanding on how the system evolves for a multi-mode perturbation. For instance, it is common to analyze the effect of amplitudes of the multi-mode waves, whereas the effect of phase of the modes constituting the initial perturbation is often ignored. From other areas of physics it is known that the relative phase is a key parameter of order and disorder (compare, for instance, white light and lasers). Following this analogy, the new model of the nonlinear RMI evolution, which takes into account both, the amplitude and the relative phase of waves constituting multi-mode initial perturbation, has been introduced by Abarzhi and co-workers (Pandian *et al*., 2016; Stellingwerf *et al.*, 2016*a*, *b*). Their model based on the group theory analysis of the confluence effects of the relative phase and amplitude of the perturbation waves, more completely describes the evolution of large-scale structures of bubbles and spikes in shock-driven RMI (Abarzhi, 2016, Private communication; Pandian *et al.*, 2016; Stellingwerf *et al*., 2016*a*, *b*).

The shock-driven RMI/RTI bubbles and spikes in the SCC are exposed to fast reshocks in different ways in different domains. In the domains of the weak reshocks, the effect on the mushroom-shape spikes and on the wave-vortex formations in the base-plane (mostly the line- and the horseshoe solitons), is small. The organization of the line solitons into polygonal web and of the horseshoe solitons into the rosette-like structure is only slightly disturbed. In the domains of strong reshocks, the effect on the spikes and on the base-plane structures is significant. The pressure variation and local pressure gradients cause the deformation of the mushroom-shape spikes and 3D flow instability with formation of stripes and vortex ribbons in the base-plane. Their interaction with deformed RTI spikes and bubbles causes formation of the low-mixing large-scale complex structures.

The paper is organized as follows: In Section 2 (*Experimental details*), short description of laser characteristics, target characteristics and of the SC configuration are given. The reference is made on the previous detail description of experiment with illustrations including the Supplement (Lugomer, 2016*a*). In Section 3 (*Results and discussion*) we study from the scanning electron microscope (SEM) micrographs of the 3D RMI/RTI morphology. The effect of the reshocks on the fluid acceleration, and formation of domains experiencing weak and strong reshock effects. In the subsection "Weak reshock effects on the RMI/RTI structures", we study the RMI/RTI spikes with damped spherical and prolate ellipsoidal mushroom shapes, and compare them with the similar mushroom shapes obtained by 3D simulation of various authors. In addition, we study the base-plane structures formed by the horizontal fluid flow that reveal large-scale low-mixing structures. We also analyze the shapes of mushroom spikes with those obtained by calculation with dependence on the Eõtvõs and Morton numbers. In the subsection "Strong reshock effects on the RMI/RTI structures", we

https://doi.org/10.1017/S026303461700009X Published online by Cambridge University Press

study the deformation of mushroom-shape spikes under strong reshocks, base-plane horizontal flow instability and formation of stripes and ribbons, interaction of flow stripes and ribbons with RMI/RTI structures, interaction of flow stripes and ribbons with bubble-cavities (holes), interaction of flow stripes and ribbons with mushroom-shape spikes that form large-scale low-mixing structures. Section 4 is *Conclusion*.

2. OUTLINES OF THE EXPERIMENT

The experiments were performed in the SCC in which the target is irradiated through transparent quartz plate positioned at $\Delta \sim 120$ μm above the target surface (Lugomer, 2016*b*). Irradiation was performed by a single pulse of a *Q*-switched ruby laser $E \sim 160$ mJ ($E_s \sim 12$ J/cm^2; $P_s \sim 0.48 \times 10^9$ W/cm^2 ($\sim$0.5 GW/cm^2); $\tau = 25$ ns, $\lambda = 628$–693 nm). Indium plates of $1 \times 1 \times 0.1$ cm^3, as a soft material with the melting point $T_M = 429$ K and boiling point $T_B = 2345$ K, were used as targets. Schematic representation of the experimental setup is given in Figure 1. For better definition of the spot size, the beam was, first expanded, and then focused by the optical focusing module (focal length, $f = 35$ cm) on the sample. The sample was situated in the gas chamber and irradiated in the presence of air as a background gas at the normal pressure $P_0 = 1$ atm (Lugomer, 2016*b*). The spot diameter was $D \simeq 1.3$ mm, and the area irradiated was $S = 0.013$ cm^2, and the radius of the spot $r = 650$ μm).

The leading edge of a laser pulse causes the ablation of indium and generates the vapor–plasma plume, which is trapped in the microchannel of the SCC like a layer about $\sim$150 μm thick. This low-density layer, ρ_L, is in contact

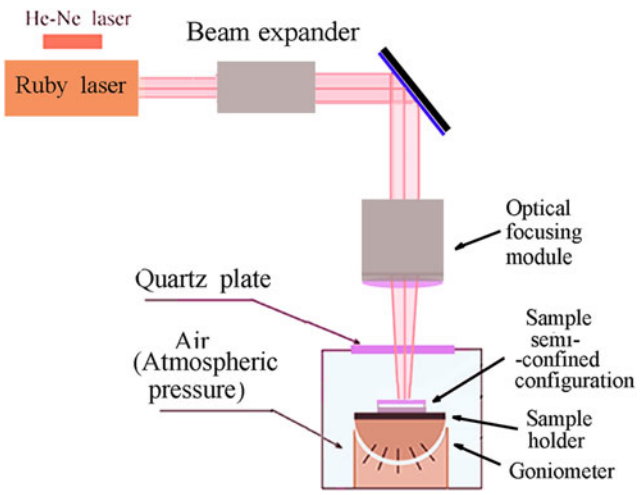

Fig. 1. Layout of the experiment and the laser beam characteristics. The beam of ruby laser is expanded and after reflection directed to the sample by the focusing module. The sample is in the SCC situated in the chamber in the presence of background gas (air, atmospheric pressure), and irradiated through the quartz window. Schematically, a small He–Ne laser is put in the geometric axis of the beam for adjustment of the sample irradiation before firing the Ruby laser.

with the high-density layer, ρ_H, of molten indium on the solid (unaffected) target thus establishing vertical density gradient. The absorption of laser energy causes subsequent plasma ignition and detonation with generation of a shock wave in the center of a microchannel. The shock-wave traveling downward strikes the ρ_L/ρ_H interface causing deposition of baroclinic vorticity. The illustration is given in Figure 1a–1d of paper I (Lugomer, 2016*b*), and also described in its Supplement. The shock-wave traveling upward is reflected as reshock from the cover plate. The reflection of the shock wave as the reshock and from the target surface, as well as the lateral plume expansion in the ambient gas are shown in Figure 1e–1h of paper I (Lugomer, 2016*b*), and the details described in its Supplement.

The growth of spikes and bubbles forms the morphology, which stays frozen permanently by the fast solidification after the termination of interaction. Since the structures are formed in the microchannel of the SCC, they experienced fast reshocks, so that *a posteriori* study by the SEM JEOL, reveals the final morphology.

3. RESULTS AND DISCUSSION

3.1. Surface morphology formed by RMI/RTI and mixing

The SEM micrograph of circular Gaussian-like spot of the RMI/RTI morphology with the excerpt of the CR and the NCR (outer ring) is shown in Figure 2. The enlarged segment of NCR in Figure 3a shows the quasi-periodic web with the mushroom-shape spikes at the average distance of $\sim$40–50 μm. Since the SEM pictures of the spikes have been taken *a posteriori*, the above distance between the spikes is therefore distance at the end of interaction.

The spike breakup (in contrast to the CR) is a minor effect [Fig. 3b (i) and (ii)]. Such morphology is the result of decrease of the *A* number from the CR ($A \sim 1$–0.85) to the NCR ($A \sim 0.85$–0.65) and of the decrease of the momentum transfer from the maximal $\boldsymbol{M} \sim \boldsymbol{M}_{max}$ (in the CR) to about $\boldsymbol{M} \sim (0.60$–$0.70)\ \boldsymbol{M}_{max}$ (in the NCR) (Lugomer, 2016*b*). Under such conditions the RMI is followed by the reversal of pressure and density gradients, which generate the RTI (Miles *et al.*, 2005; Suponitsky *et al.*, 2013, 2014; Lugomer, 2016*b*); the interface perturbations grow into spikes of heavy-fluid into light-fluid and bubbles of light-fluid into heavy-fluid.

The 3D quasi-periodic web may be compared with numerically simulated regular periodic morphology. The 3D simulated large-scale periodic RMI structures were generated by both, the single-mode (Miles *et al.*, 2005; Long *et al.*, 2009) and the multimode perturbations (Cohen *et al.*, 2002; Kartoon *et al.*, 2003). An example is the large periodic structure obtained for the vertical interface oscillation in a square cell due to the single-mode 3D perturbation

$$z(x, y) = a_0 \cos(k_x x) \cos(k_y y), \quad (1)$$

https://doi.org/10.1017/S026303461700009X Published online by Cambridge University Press

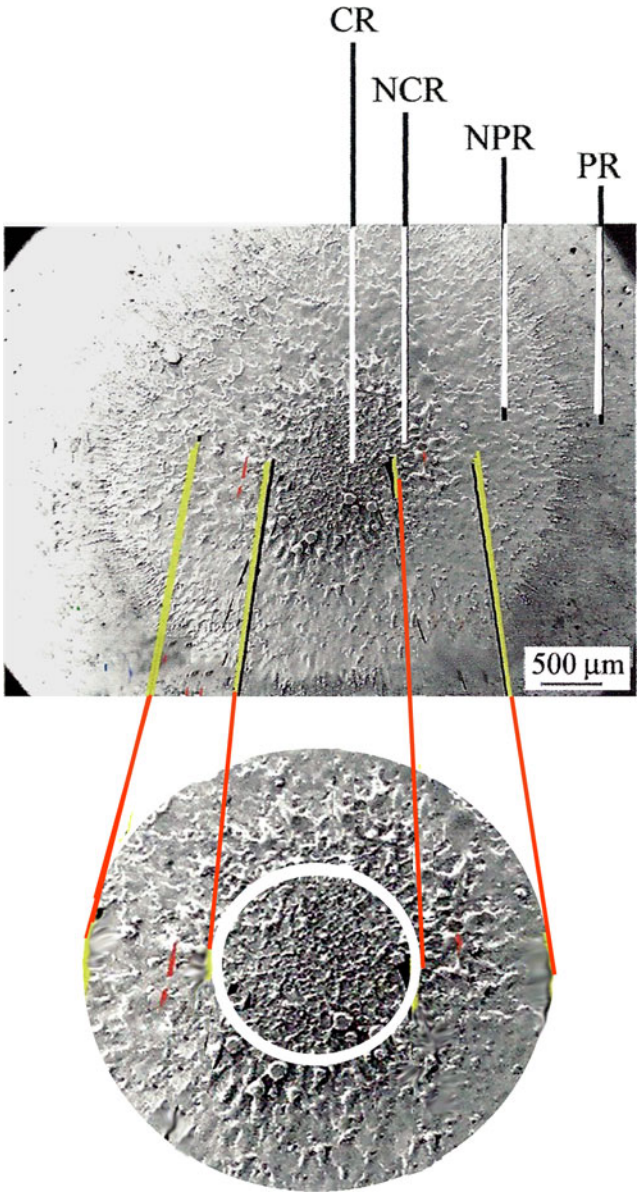

Fig. 2. SEM micrograph of the spot on indium surface after irradiation by a circular laser beam with Gaussian-like laser power distribution. Note the formation of four circular regions: the CR, NCR, NPR, and the periphery region (PR). The morphology of the NCR (outer ring) is better seen in the magnified excerpt from the spot.

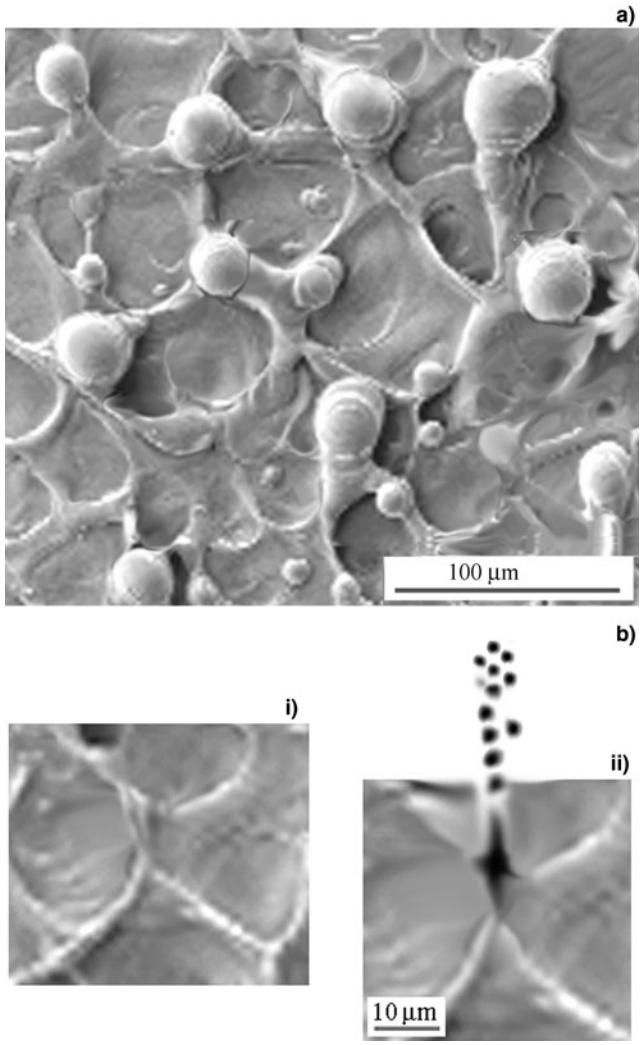

Fig. 3. SEM micrograph of the NCR corresponding to the random flow field (*incoherent domain*) caused by the RMI/RTI turbulent mixing. (a) SEM micrograph showing a dominant morphology of the NCR; the irregular (broken) "egg carton" web with the RTI mushroom-shape spikes at the nodal points and the cavities (collapsed bubbles). The irregular "walls" around the bubbles are connected into a web corresponding to 2D deformed lattice. (b) SEM micrographs showing the minor type of morphology of the NCR: the jet-spike breakup similar to the CR (Lugomer, 2016*a*). The surface morphology after the RMI jet spike breakup (i). Breakup of turbulent jet-spike leaving only the "walls" on the surface (ii).

where $a_0 = 3.45$ mm, $k_x = k_y = \sqrt{2}\,\pi/W$, and $W =$ width of the test section, for the weak shock of $Ma = 1.22$ and the low Atwood number $A = 0.65$ (Long *et al.*, 2009). Transformation of a regular periodic web into deformed one (broken) may be attributed to the bubble shape oscillations driven by the fast oscillatory reshocks (Lugomer, 2016*b*), and to the effect of the reshocks on the fluid shear layer. The laterally accelerated shear layer expands from the CR into the NCR with the velocity $U \sim 1650$ m/s (the sonic velocity in liquid indium), and suffers variation of thickness and velocity due to reshocks. The reshocks gradually become oblique and randomly oriented (due to irregularity of the interface), increasing the inhomogeneity of the fluid flow field. All fluid parameters become more or less affected; the density ratio ($\rho g/\rho l$; $g =$ vapor/plasma gas, $l =$ liquid indium), viscosity ratio ($\mu g/\mu l$), the A number, the Re number, etc. In such flow field, two types of domains of the NCR can be roughly distinguished: the domains of the weak reshock effects, and the domains of the strong reshock effects on the RMI/RTI mushroom-shape spikes and the base-plane structures.

3.2. Weak reshock effects on the RMI/RTI structures

The foregoing division of the inhomogeneous flow field into two types of domains we continue with the analysis of the

https://doi.org/10.1017/S026303461700009X Published online by Cambridge University Press

weak reshock effects, which only slightly affect RMI/RTI structures: mushroom-shape spikes (damped-, spherical, and elliptical), and the base-plane wave-vortex structures.

3.2.1. *Damped mushroom-shape RTI spikes*

The *damped spherical mushroom spikes* of diameter ~15–30 μm and two vortex rings surrounding the spike – one scarcely seen and the other larger deformed-ring – are shown in Figure 4a–4c. The size of deformed ring increases from (a) to (b) and to (c), while of the surroundings decreases; the deformed ring becomes larger and stretches the smaller one (Fig. 4c). The horseshoe type base-plane structures are self-organized (SO) into the rosette-like configuration, which is slightly perturbed by the weak reshocks. The horseshoe structures are the parabolic-like solitary waves, similar to that in the CR (Lugomer, 2016*b*). The straight-line structures with the bell-shaped profile are – *the line solitons* – while the others are *cnoidal waves* (Fig. 4d). Some of the line solitons in Figure 4 (a – upper left; b and c – down right) interact between themselves giving rise to the resonant "Y-junction" configuration. The roll-up of the waves into vortex filaments occurs in the segments where the *Re* number reaches the critical value, $Re \geq Re_{crit}$ ($\sim 2.3 \times 10^3$), while those with $Re < 10^3$ show the formation of nonlinear waves.

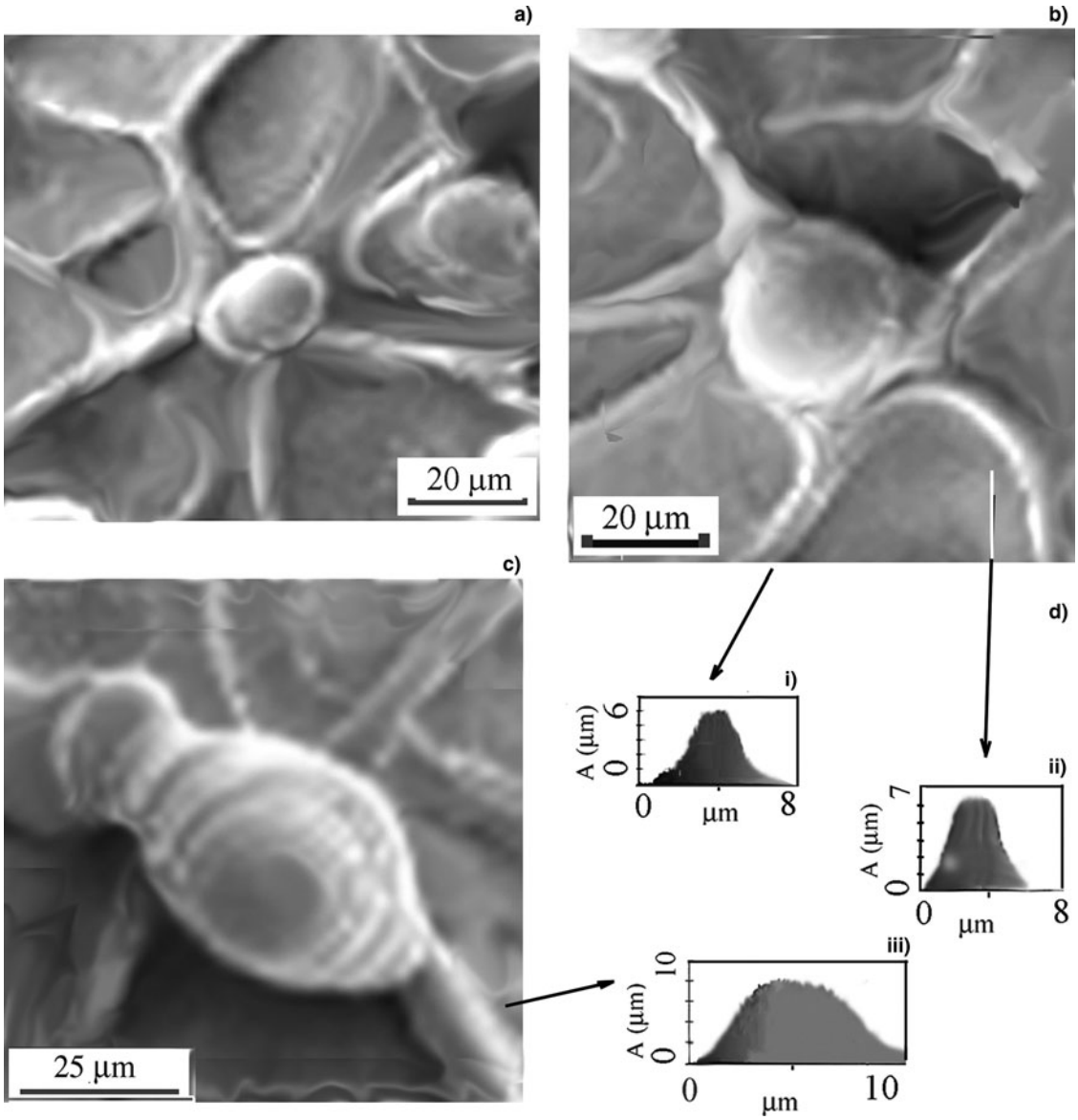

Fig. 4. SEM micrograph of the small *partially-coherent-domains* inside random flow field showing the SO of the horseshoe structures into the rosette-like configuration (a–c). The symmetry of the rosettes is disturbed due to partial coherence of the flow field in the domains. Note that every rosette comprises a *damped mushroom-shape* spike and two vortex rings. The size of damped mushroom-shape spike increases from (a) to (b) and to (c). Simultaneously, the stronger ring increases in size and becomes more deformed at the expense of the weaker one. (d) SEM profiles of radial structures of the rosettes: The bell shape profile indicates solitary waves (i, ii); the hump-like indicates cnoidal waves (iii).

https://doi.org/10.1017/S026303461700009X Published online by Cambridge University Press

The amplitude of the spikes $h_s \sim 20$–25 μm, and of the bubbles $h_B \sim 18$–20 μm gives $h_S/h_B \sim 1$, indicating approximately the same growth rate of damped mushroom spikes and bubbles.

The comparison of *damped spherical mushroom spikes* in Figure 4a–4c with those obtained by 3D numerical simulation of RMI turbulent mixing for the lower Atwood and the Mach numbers, shows a great similarity. In particular, the single-mode initial perturbation with $A = 0.65$ and $Ma = 1.2$ (Long *et al*., 2009), generates the spike with a *damped mushroom cap* and two vortex rings, one of them just above the base-plane. The deformed vortex ring around the spike stretches the weaker one into deformed configuration, similar to that in Figure 4a–4c. Generally, the characteristics of the rings depend on the A number. At the very low A ($A = 0.15$) flow instability possess symmetric features in the formation of vortex rings (Chapman & Jacobs, 2006), whereas with a higher A the flow losses this symmetry and at $A = 0.65$ the vortex ring becomes deformed (Long *et al*., 2009).

3.2.2. *Spherical RTI mushroom-shape spikes*

Many domains of the NCR show *spherical mushroom spike*, which is an indicator that the dynamics is isotropic in the plane normal to acceleration. Below the mushroom the vortex ring (or even two rings) of radius $R \sim 15$ μm and the core diameter of $\sigma \sim 3$–4 μm, surrounding the spike can be seen (Fig. 5a). Based on the above discussion the rings surrounding the spike generated at $A \geq 0.65$ should be deformed and seen at the high resolution only (Long *et al*., 2009). However, the rings in Figure 5a formed at $A \sim 0.85$–0.65 are rather regular indicating dependence on some other parameters, as described latter on.

The four radial structures divide the base-plane into four angular segments. The (wall) border-lime between the segments (i) and (ii) is the pair of two vortex filaments under an angle of $\alpha \leq 3^0$ with the *intersection in the nodal point*. The segments (i) and (ii) show only a small depression (cavity) without a hole. The radial structures at the border of the segments (ii)–(iii) and (iii)–(iv) are joined *in the nodal point* at the base-plane. Finally, the border of the segments (i)–(iv) is the terrace-like wave formed by the pulsating flow due to the reshocks and accumulation of material. The surface depression and the hole in the segments (iii) and (iv) are formed by the bubble collapse near the solid target surface, so that the hole is created by the reentry jet (Lugomer, 2016*b*). Various radial structures in the base-plane in Figure 5a, like the nonlinear waves and the vortex filaments result from the inhomogeneous fluid acceleration. In such field, the fluid flow which does not reach the critical *Re* number forms the nonlinear waves, while that reaching the Re_{crit} is rolled up into vortex filaments or the Kelvin-Helmholtz (KH) rolls. The near-circular cross-section through the single KH roll for $Re > Re_{crit}$ ($\sim 2.3 \times 10^3$) in Figure 5b, formed at the mid-span plane of interfacial surface between the high-speed free-stream fluid (blue) and the low-speed one (red), reveals the low mixing (Koochesfahani & Dimotakis, 1986; Dimotakis, 2000; Zhou *et al*., 2003). The cross-section through two pairing vortex rolls (Fig. 5c) (Koochesfahani & Dimotakis, 1986), is a good representation of the cross-section through the pair of vortex filaments at the border between the segments (i) and (ii) in Figure 5a. Thus, even in the late phase the transformation of the large-scale low-mixing structures into the small-scale turbulent mixing does not take place.

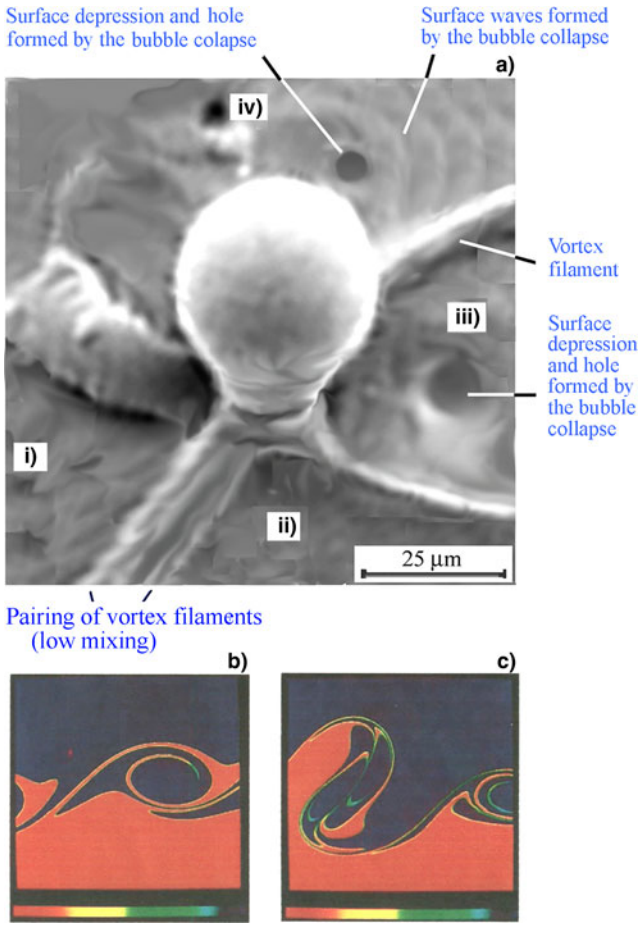

Fig. 5. Small *partially-coherent-domain* inside random flow field. (a) SEM micrograph showing the *spherical mushroom-shape* spike with two vortex rings below the mushroom cap. The structures in the base-plane (interface: saddle point plane), are the radial straight-line structures identified as the nonlinear waves and cylindrical vortex filaments organized into polygonal (square-like) web. The borders of the polygonal web divide the base-plane into four angular segments (i–iv). For the characteristics of the border-lines between the segments see text. Illustration of the cross-section through the vortex filaments by digital laser-induced florescence (LIF) streak images: (b) Digital LIF streak image showing low mixing for almost circular cross-section through the single cylindrical vortex filament rolled up at the density interface for $Re = 1750$. (c) Almost circular cross-section through two pairing cylindrical vortex filaments for $Re = 1750$. (Courtesy of Professor Koochesfahani M.M. and Dimotakis, P.E. Reproduced with permission of Cambridge University Press from, Koochesfahani & Dimotakis (1986). Copyright Cambridge University Press, 1986).

The absence of the small-scale turbulence at the late times is a complex problem and requires few more words. For the

https://doi.org/10.1017/S026303461700009X Published online by Cambridge University Press

experiments performed in SCC, it expected to show the same behavior of RMI/RTI structures as those in the open configuration. It means that the large-scale low-turbulent structures formed at the early times of interaction should vanish and the small-scale structures should appear (characteristic for the late times) after reshocks. Such behavior by a number of respected authors (Cohen *et al.*, 2002; Anuchina *et al.*, 2004; Miles *et al.*, 2005; Long *et al.*, 2009; Youngs, 2013), etc. Even more, the transition to the small-scale highly-turbulent structures in their pictures is observed not only on the base-plane, but also on the mushroom-shape spikes. The examples are Figure 5 of Long et al. (*2009*) especially between 5.96 and 11.43 ms, and also Figure 6 (Anuchina *et al.*, 2004) between 0.064 and 0.108 ms, as well as Figures 7 and 8 of Schiling and Latini between 8 and 11 ms, etc. Even more, they reveal the formation of the cascade from the large to the small-scale structures indicating self-similarity. The mushroom spikes in their above-motioned pictures become highly disturbed and show break down into small-scale high-mixing turbulence as the stochastic process.

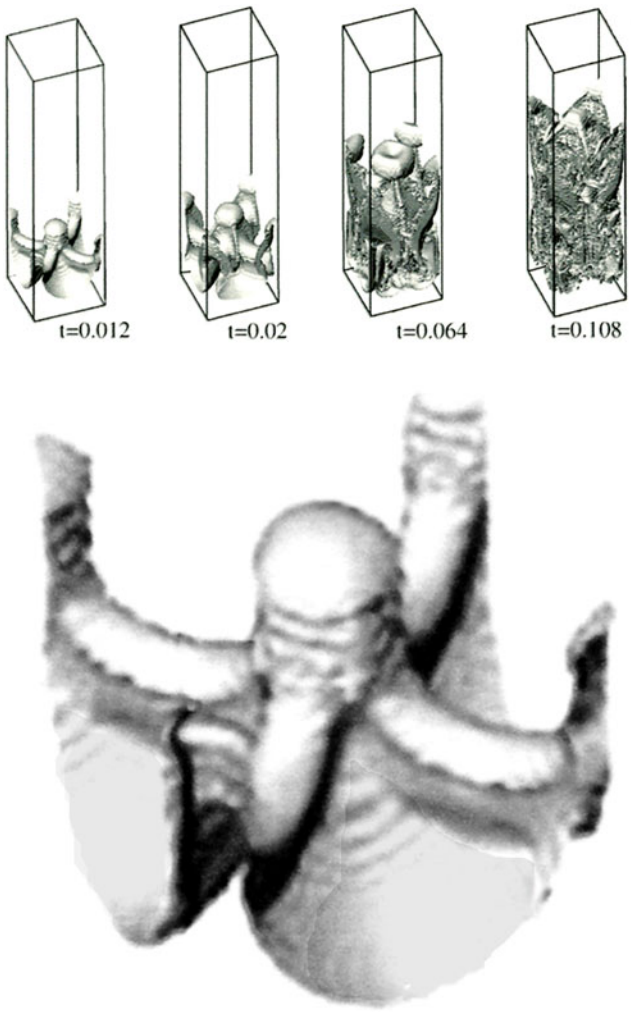

Fig. 6. 3D numerical simulation of the perturbation development into the spherical mushroom-shape spike and diagonal structures in the time sequences $t = 0.012$ ms, $t_2 = 0.02$ ms, $t_3 = 0.064$ ms; $t_4 = 0.108$ ms (Bottom). The enlarged mushroom-shape spike developed at $t = 0.012$ (the first calculation box) can be favorably juxtapositioned with the experimental one in Figure 4. (Reproduced with permission of Elsevier from, Anuchina *et al.* (2004); Copyright Elsevier, 2004).

However, Figures 4, 5a, 7 (taken at the end of experiment, i.e. at the late times), do not show the expected onset of small-scale structures. Instead, they show large spherical and ellipsoidal mushroom spikes with the smooth surface without any indication of break down into smaller structures. In the base-plane, they show nonlinear waves and vortex filaments of the core size of ~5–7 μm, and ~50 μm long as the large-scale coherent structures with quasi-regular or chaotic organization.

The tentative interpretation may be that interfacial RMI/RTI mixing in the SCC is somewhat different from the usual canonical turbulence, which is an equivalent of a stochastic process. In such process, the flow fluctuations are independent of the initial conditions, boundary conditions, and external forcing. For canonical turbulence to occur the conditions of isotropy, locality, homogeneity, and statistical steadiness should be fulfilled (Abarzhi, 2016, Private communication). The micrographs in Figures 4, 5a, and 7 indicate that such conditions in SCC are not fulfilled or they are disturbed, so that the RT and RM mixing flows do not form the small-scale structures. It seems that their sensitivity to the initial conditions suggests that mixing is more "chaotic" rather than stochastic processes (Abarzhi, 2016, Private communication).

The comparison of *spherical mushroom spike* in Figure 5a shows a great similarity with 3D numerical simulation of RMI/RTI for the multicomponent flow at the high Atwood and Mach numbers. A single-mode sinusoidal perturbation for $A = 0.82$ and $Ma = 2.5$, generates the spherical mushroom spike with vortex rings and four diagonal structures in the base-plane (Anuchina *et al.*, 2004) (Fig. 6). The spherical mushroom spike appears at the short simulation times between $t = 0.012$ and 0.02 ms. At magnification, the mushroom spike with vortex rings in Figure 6 (down), shows the similarity with that in Figure 5a in more detail.

Diagonal structures in the base-plane (Fig. 6) are vortex structures which form four identical segments similar to that in Figure 5a. The shock-wave propagation through the sinusoidally perturbed interface causes the formation of vortex structures. In 3D simulation, the perturbation has different wavelengths in the diagonal directions from the cross-sections what leads to the earlier termination of the shock interaction with the interface in the diagonal sections (Anuchina *et al.*, 2004). The *vortex platens* (the raised flat "walls" at the base-plane) are formed by the termination of the shock-wave refraction in the diagonal section of the simulation cell at $t_1 = 0.012$ ms. The subsequent formation of reflected shock waves causes impact at the cross-platens at $t_2 = 0.020$ ms, causing the roll-up and formation of *vortex filament crosspieces* (Fig. 6). At the latter stages (at $t_3 = 0.064$ ms), the roll-up does not increase. Instead, the interaction of the next-generation waves among themselves and with the vortex formations takes place and initiates the

https://doi.org/10.1017/S026303461700009X Published online by Cambridge University Press

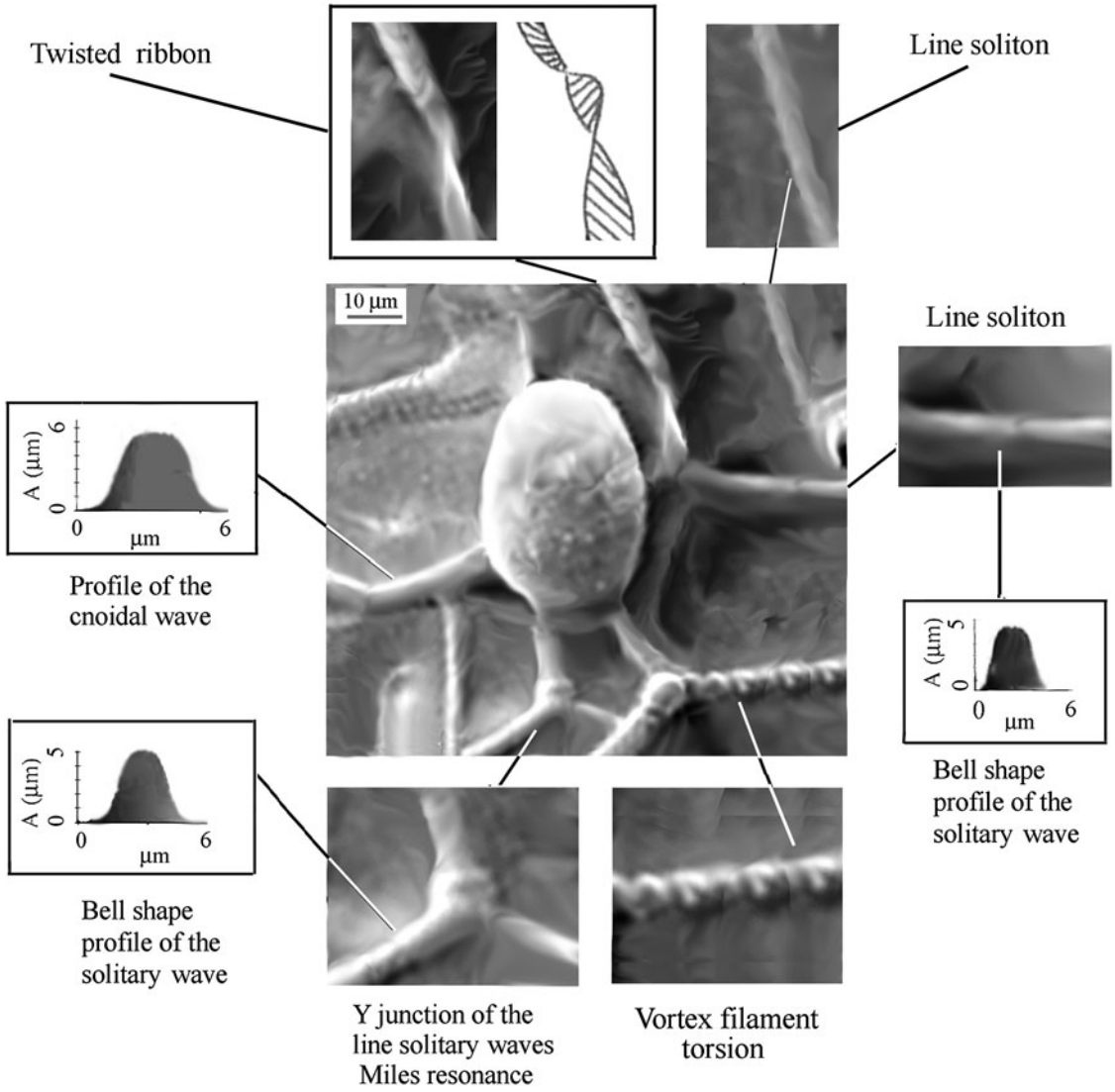

Fig. 7. SEM micrograph of the small *partially-coherent domain* inside random flow field showing the *prolate ellipsoidal mushroom-shape spike* without vortex rings below the mushroom. The straight-line structures in the base-plane (interface: saddle point plane) are the cnoidal waves (upper left), while the others (lower left and middle right) are the line solitary waves and vortex filaments SO into the irregular polygonal web. The upper structures are vortex ribbons, while the bottom structures are the line solitons, which interact and form the resonant "Y-junction" configuration.

final small-scale turbulent mixing as seen in Figure 6 at t_4 = 0.108 ms (Anuchina *et al.*, 2004).

Consider the growth rate of the experimental spherical mushroom spikes and bubbles. The spike amplitude $h_S \sim 30$ μm, and of the bubbles $h_B \sim 18$ μm ($h_S/h_B \sim 1.66$, $h_B/h_S \sim 0.6$), indicating that spikes grow somewhat faster than bubbles but slower than for the nonlinear multimodal perturbation since $h_S/h_B < 3$ ($h_B/h_S \sim 0.3$–0.4) (Alon *et al.*, 1996). The fact that 3D-simulated RMI spherical mushroom spike in Figure 6 generated by the single-mode perturbation of Anuchina *et al.*, is very similar to the experimental one in Figure 5a generated by the multimode perturbation, leads to the tentative conclusion. In the multimodal perturbation, only one – or few modes of close wavelengths (band of modes) – causes the formation of a spherical mushroom spike what makes it similar to that formed by the single perturbation mode. However, the another possible interpretation (which is more appropriate) indicates that interference of perturbation modes, which generates the resulting one, causes the formation of a spherical mushroom spike as shown by Abarzhi and co-workers (Pandian *et al.*, 2016; Stellingwerf *et al.*, 2016*a*, *b*). By using the group theory analysis and the Smooth Particle Hydrodynamics numerical simulations they have shown that symmetry of the coherent RMI pattern depends besides the amplitude of the waves also on their relative phase. As a result, the wave interference influences symmetry, morphology, and growth rate of the spikes and bubbles at the interface.

3.2.3. *Prolate ellipsoidal RTI mushroom-shape spikes*

Some of the domains of the NCR show the RTI *prolate ellipsoidal mushroom spike* (with the small axis of ~20 μm

https://doi.org/10.1017/S026303461700009X Published online by Cambridge University Press

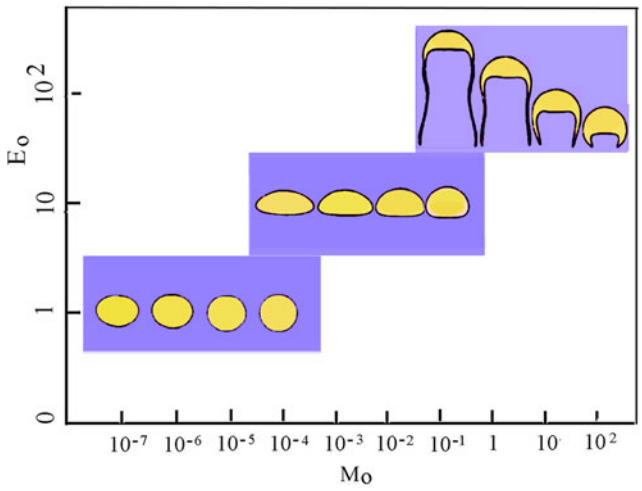

Fig. 8. The steady state of a rising mushroom bubble for the ratio of densities, $\rho_l/\rho_b = 40$, as function of the Eötvös, *Eo*, and Morton, *Mo*, numbers. The values of the viscosity ratio, μ_l/μ_b, in the rows from left to right. Bottom row: 85; 151; 269; 479. Middle row: 88; 156; 277; 493. Top row: 88; 156; 277; 493 [the origin of the data is the paper: Unverdi & Trygvason (1992)].

and the long one of ~35–40 μm), without the KH vortex ring around the spike (Fig. 7). The comparison of elongated prolate mushroom spike with 3D simulation of such spikes is not very favorable. Namely, the simulation performed for the high *A* number ($A = 0.9$) gives the elongated 3D mushroom spike for the late times ($t = 2.5$) (He *et al.*, 1999). However, it is not the prolate ellipsoid, but the elongated spike spherical on top and flat on the bottom. Similarly, the 2D simulation generates also the elongated mushroom spike for the same late times ($t = 2.5$), but not the prolate ellipsoid (Zhang *et al.*, 2006). According to He *et al.*, the elongated mushroom formation results from the symmetric variation of the horizontal growth rate, which increases with increasing height until the equatorial maximum is reached; then the horizontal growth rate starts to decrease thus forming the symmetric elongated mushroom (He *et al.*, 1999). The mushroom is symmetric with respect to the vertical and the horizontal cross-sections. In the case of simulation, the horizontal growth (velocity) is large and stays almost constant with growing vertical in the *z*-direction, until the top rounded surface starts to form. Thus, the mushroom is symmetric with respect to the vertical cross-section and asymmetric with respect to the horizontal one (He *et al.*, 1999). This rather general description is valid for all types of the elongated spikes, but does not elucidate their origin, especially not of the prolate one, and at present, its formation is not quite clear.

Consider the growth rate of experimental spikes and bubbles. The amplitude of the spikes $h_s \sim 30$–35 μm and of the bubles $h_B \sim 10$ μm with $h_S/h_B \sim 3$–3.5, indicating three times faster growth rate of the prolate ellipsoidal spikes than of bubbles. This result is in agreement with the growth rates of RMI spikes and bubbles for the nonlinear multimodal perturbation, assuming that all incommensurate modes take place in the formation of structure (Alon *et al.*, 1996). However, regarding the spike dynamics in the light of empirical, semi-empirical and engineering models (such as Layzer-type, drag model Alon *et al.*, 1996; Zhang's model, 1998, etc.), more caution is required. As a matter of fact, at present there is no a rigorous theoretical description of the dynamics of nonlinear spikes. On the theory side, the empirical models often have many limitations (such as unphysical velocity fields, non-existing mass fluxes, etc.) that are not confirmed in experiments. Extensive use of adjustable parameters enables the models agreement with experiments (Abarzhi, 2016, Private communication).

The base-plane in Figure 7 (upper left) comprises the straight "walls" with the profile of *cnoidal waves*, while the other "walls" (lower left) as well as those on the right side of the micrograph have the bell-shape profile of line solitons. The line solitons observed at the lower side interact and form the resonant "Y-junction" configuration (Kodama, 2004; Oikawa & Tsuji, 2006; Lugomer *et al.*, 2013; Lugomer, 2016*a*). (For details see the paper, Lugomer, 2016*b*, and for the mathematical aspects, Kodama, Oikawa, Biondini). A variety of wave-vortex structures indicates that the fluid dynamics in the base-plane is inhomogeneous and causes complex formations. An example is the anchored vortex filament with the spiral-like structure exposed to torsion (Fig. 7, lower right side). Another example is the flattened vortex filament (upper left side) transformed by twisting into twisted-ribbon (Lugomer & Fukumoto, 2010).

3.2.4. *Damped, spherical, and elongated RTI mushroom spikes*

The shape variation of damped, spherical, and the prolate ellipsoidal mushroom-shape spikes in Figures 4, 5a, and 7, cannot be attributed to the variation of the *A* number only. Description of the mushroom-shape variation requires characteristics of the system, like the density ratio (ρ_l/ρ_b) and viscosity ratio (μ_l/μ_b), where index, *l*, relates to liquid and, *b*, to the bubble (gas), to be taken into account. Variation of the RTI mushroom shapes has been studied by numerical simulation for bubbles in a viscous liquid (Hua & Lou, 2007), in the RTI (Unverdi & Trygvason, 1992), and under different flow conditions with incorporation of the force term (Shu & Yang, 2013). These models describe the gas–liquid system in which the density (ρ_l) and the viscosity (μ_l), are used for definition of the additional parameters like the Eötvös number, *Eo*, and the Morton number, *Mo*. The Morton number involves the fluid properties only, and the Eötvös number is the nondimensional size of the bubble. The bubble shape can be characterized by the Morton number, $Mo = g\mu_l^4/\rho_l\sigma^3$, by the Eötvös number, $Eo = \rho_l g d_l^2/\sigma$ (also called the Bond number), and by d_l, the effective radius of the bubble (Unverdi & Trygvason, 1992). The rate of rise (growth) is expected as the Reynolds number in terms of the rise velocity, $Re = \rho U d_l/\mu$, where *U* is the velocity. Often the Weber number, $We = \rho U d_l/\sigma$, is also used to characterize the bubble.

https://doi.org/10.1017/S026303461700009X Published online by Cambridge University Press

In the analysis of the mushroom-shape variation, we rely on the simulation of Unverdi and Trygvason for the mushroom bubble shapes in RTI (Unverdi & Trygvason, 1992). The analysis is based on the Boussinesq approximation for the buoyant bubbles where two fluids have dependence on the surface tension and difference of densities of the fluid inside the bubble and the surrounding fluid (Unverdi & Trygvason, 1992). The resulting diagram of the mushroom shapes as function of the *Eo* and *Mo* for the constant density ratio ($\rho_l/\rho_b = 40$), is shown in Figure 8. The diagram shows mushroom shapes for the *Eo* ranging from 1–10^2, and *Mo* number ranging from 10^{-7} to 10^2 (Unverdi & Trygvason, 1992). The viscosity ratio, μ_l/μ_b, for every particular case is given in the caption to Figure 8.

For small Eo (*large surface tension or small bubble*), the RTI bubbles are almost spherical (bottom row) (Fig. 8). However, for small *Eo* and small *Mo* the bubble front is slightly flatter than the back (bottom row, left), while for the small *Eo* and higher *Mo* the bubbles become more spherical (bottom row, right).

For higher Eo (*transition zone from small to large bubbles*), the bubbles attain somewhat flat shape (middle row). If the *Mo* is low (middle row, left), then the bubbles become ellipsoidal (Fig. 8). With increasing *Mo* the bubble front becomes semi-circular while bottom becomes more flat (middle row, right). For the high *Mo* the bubbles become ellipsoidal.

For the highest Eo (*small surface tension or large bubbles*), the solution is not truly steady state; the skirts of the bubbles are pulled off with a separated flow increase continuously in length (top row, left) (Fig. 8). The vertical rise of the bubble is independent of the *Mo* number; for largest bubbles the pressure drag and the velocity are independent of the viscosity (Unverdi & Trygvason, 1992).

The *Eo* and *Mo* numbers for the mushroom shapes in Figures 4, 5a, and 7 may be estimated from the comparison with the calculated shapes in Figure 8. The damped mushroom-shapes in Figure 4a–4c ($A \sim 0.65$), are similar to the shapes in Figure 8, for $Eo \gtrsim 10$ and $10^{-4} \leq Mo \leq 10^{-1}$. The prolate ellipsoidal mushroom shape in Figure 7 is similar to the bubbles-with-skirts for $Eo \gtrsim 10^2$ and, $10^{-1} \lesssim Mo \lesssim 1$, while the spherical one in Figure 4a ($A = 0.85$) is similar to the spherical mushroom for $Eo \gtrsim 10^2$ and $Mo \sim 10^2$.

3.2.5. *Low-mixing structures in the base-plane*

The base-plane structures in Figures 4, 5a, and 7 – mostly the nonlinear waves and vortex filaments – are the large-scale formations with diameter (core size $\sigma \sim 3$–6 μm), and the length $L \sim 30$–40 μm. These coherent formations are organized into various configurations: the nonlinear horseshoe waves – into the rosette-like structures, and the line solitary waves – into the polygonal web. The horseshoe waves are similar to those in the CR (Lugomer, 2016*b*), and identified as the parabolic-like solitary waves, which were studied by various mathematical groups on the basis of the cyllindric Kadomtsev–Petviashvilli equation (Klein *et al.*, 2007; Khusnutdinova *et al.*, 2013; Lugomer, 2016*b*). The straight-line structures with the bell shape profile are – the *line solitons* – while the others are *cnoidal waves* [Fig. 4(iv)]. The line solitons interact between themselves giving rise to the "Y-junction" or the "X-junction", etc. as the resonant and nonresonant configurations, respectively (Kodama, 2004; Oikawa & Tsuji, 2006; Biondini, 2007; Lugomer, 2016*b*). The other radial structures are *vortex filaments* formed by the roll-up of the nonlinear waves. The roll up into KH filament-rolls occurs in the segments where the *Re* number reaches the critical value $Re \geq 10^3$. These base-plane structures show only the low mixing, which stays to the late times and does no show transition to the small-scale turbulent mixing.

The 3D RMI simulations reveal transition from the large-scale low-mixing to the small-scale well-developed turbulent mixing with randomly oriented structures at the late times (Anuchina *et al.*, 2004; Long *et al.*, 2009). Such structures are characteristic for the statistically random distribution of velocity, density, or temperature (Zhou *et al.*, 2003). Thus, the late time, low-mixing, large-scale structures of nonlinear waves, and vortex filaments in Figures 4, 5a, and 7, can be compared with the similar simulated ones existing only for the short times. In the experiment, the large-scale structures persist to the late times when the solidification of target surface takes place (~200 μs after pulse termination). The transition to the small-scale turbulent mixing is frustrated (prevented) most probably because of the interaction with the nonstationary flow in the base-plane (Zhou *et al.*, 2003); and because of the collapse of bubbles, which generates the shock waves into the surrounding fluid that wipe out the small-scale structures. The existence of the large-scale structures even at the late times indicates the lack of turbulent mixing with statistically random distribution of velocity or density. Thus, the paradigm of the nonlinear low-mixing wave-vortex structures characterizes the RMI/RTI in the NCR.

3.3. Strong reshock effects on the RMI/RTI structures

Strong reshocks have very dramatic effect on the mushroom-shape spikes and on the base-plane structures. Under the series of reshocks, the location of the interface moves downward. As a result, the complexity of the structures increases by deformation and with breakup of their symmetry.

3.3.1. *Deformation of mushroom-shape spikes*

Deformation of the mushroom-shape spikes and breakup of their symmetry is shown in Figures 9a(i, ii), which can be compared with the simulated ones for the initial RT mixing layer (Zhang *et al.*, 2006). Their 2D simulation of the shock effect on RT structures at $Ma = 6$, shows the evolution of deformation and symmetry breakup in $t = 1.6$, 1.85, 2.3, 2.6, and 3 (Fig. 9b). The great similarity with mushroom structures in Figure 9a is observed for $1.6 < t \leq 2.6$. The deformation occurs when the interface with the shock wave

https://doi.org/10.1017/S026303461700009X Published online by Cambridge University Press

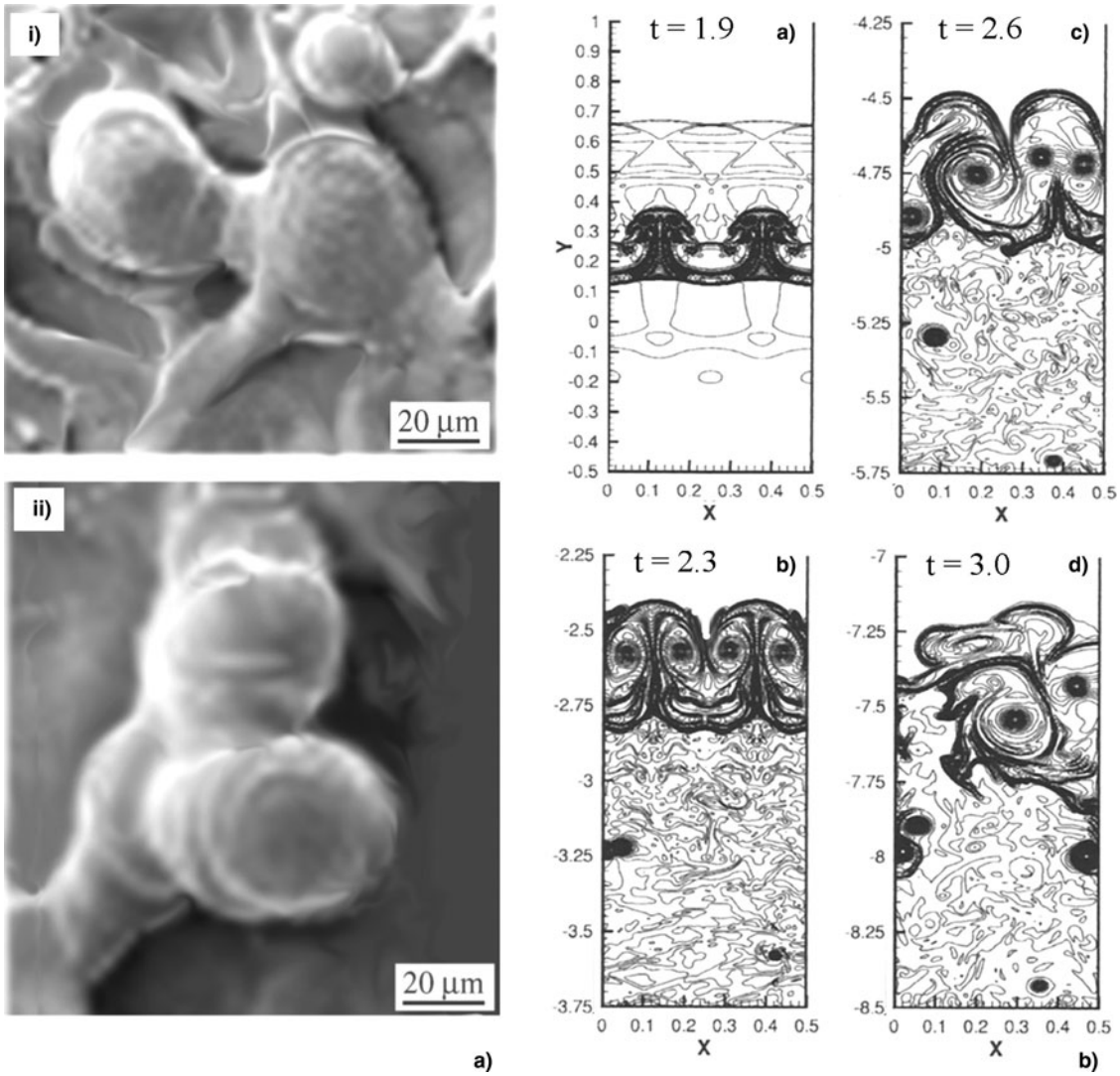

Fig. 9. The effect of a strong reshock on the RT-mushrooms and horizontal base-plane structures. (a) SEM micrograph of RTI mushroom-shape spikes showing deformation, breaking of the symmetry between them and disordered fluid flow in the base-plane. (b) Numerical simulation of strong shock effects on the RTI mushrooms. The shock hits the RT interface at $t = 1.85$ and causes strong deformation, which evolves in time: (a) $t = 1.9$; (b) $t = 2.3$; (c) $t = 2.6$; (d) $t = 3.9$. Note the similarity between deformation of mushrooms in Figure 7a and simulated ones for $1.6 < t \leq 2.6$. [Courtesy of Dr. Y-T. Zhang. Reproduced with the permission of AIP Publishing from Zhang *et al.* (2006); Copyright AIP, 2006.]

moves downward (from above) (Zhang *et al.*, 2006). If the *Ma* number of the shock is low the symmetric organization of two mushroom structures is not perturbed. Increasing the *Ma* number the symmetry is broken and the structures enter turbulent mixing and merging. The insight into this process is obtained from the temperature, entropy, and vorticity measurement (Zhang *et al.*, 2006). In the moment when the shock hits the interface ($t = 1.85$), the temperature field is divided along the shock location. The mushroom structures have not yet changed from their original entropy values, and the vorticity is small. After the passage of the reshock ($t = 1.9$), the temperature and the entropy of the mushroom structure increase rapidly with enhanced vorticity (Zhang *et al.,* 2006). However, the temperature and the entropy are different at different locations. Below the mushroom they are lower and the flow structures are stable. At the top of the mushroom the entropy and temperature are higher indicating the higher energy level and instability that leads to the breakdown of flow structures into smaller ones (Zhang *et al.*, 2006).

The simulation gives the evidence that the motion of the interface continues until the mushroom structures are broken into small turbulent pieces and merged with the base-plane vorticity making a small-scale fully turbulent mixing layer with stochastic distribution of temperature, density, and entropy (Zhang *et al.*,). In contrast, Figure 9a shows that the downward motion of the interface is stopped at some small distance above the base-plane without of the onset of small-scale turbulent mixing. Thus, the mushroom-

https://doi.org/10.1017/S026303461700009X Published online by Cambridge University Press

shape structures – although deformed – stay above the base-plane without transition to fully developed turbulence.

3.3.2. *Formation of stripes and ribbons in the base-plane*

The base-plane structures, namely the "egg carton" walls, under reshoks also suffer deformation and symmetry breakup [Fig. 10(i)]. The most dramatic effect is vanishing of the "walls", the increase of their size and spreading, as well as their splitting into three or more stripes. Under spanwise perturbation the stripes are transformed into vortex ribbons [Fig. 10(ii, iii)]. The longer ribbons tend to tangling due to transversal perturbation [Figure 10(iv)].

3.3.2.1. Interaction of flow stripes and ribbons with RMI/RTI structures. The stripes and ribbons interact with the RTI mushroom spikes and bubbles, which may be assumed the surface "point defects" characterized by their "trapping potential". Depending on the trapping potential, various complex configurations may be formed by the ribbon cyclic motion around the bubble (hole), looping around the spikes, and pinning at the base of the spike (Lugomer *et al.*, 2007). Looping of the vortex filament (ribbon) around the spike or bubble (point like defects) can be interpreted on the basis of the Pedrizzetti model (Pedrizzetti, 1992), and pinning at the spike on the basis of the Schwartz model of pinning at protrusions (Schwarz, 1985).

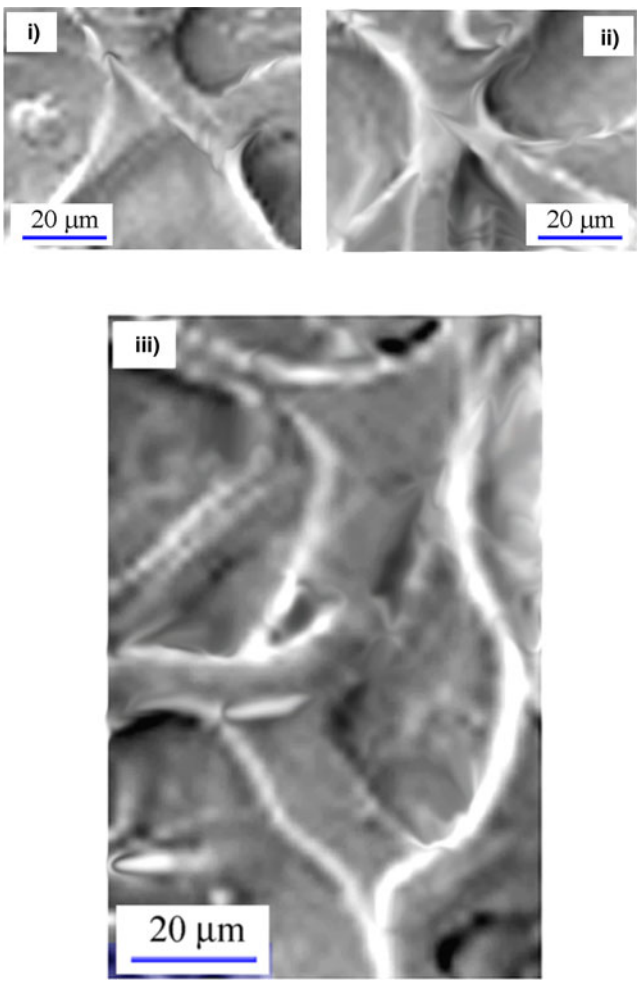

Fig. 10. SEM micrographs of the domains experiencing strong reshocks show breakdown of the "egg carton" web in the base-plane. Transformation of the former "walls" of the web between the RTI mushroom spikes into various structures by spreading and deformation (i), by splitting and the roll up into vortex ribbons due to transversal perturbation (ii, iii), and tendency to tangling of ribbons due to spanwise perturbation (iv).

3.3.2.2. Interaction of flow stripes and ribbons with bubble-cavities. Figure 11a(i) shows two vortex filament ribbons (incoming from above), one directed to the left and other the right side, which enter the cyclic motion around the cavity of a collapsed bubble; one forming a loop and other spiraling down to the hole in the center of the cavity. The ribbon structures in the vicinity merge with the ribbon loop. More complex configuration arising from the ribbon trapping with formation of closed loops and knotted structures around cavities (point defects) can be seen in Figure 11a(ii).

Point defects and trapping potential. The point defects are assumed all structures on the target surface such as holes, droplets, or other structures of spherical or hemispherical

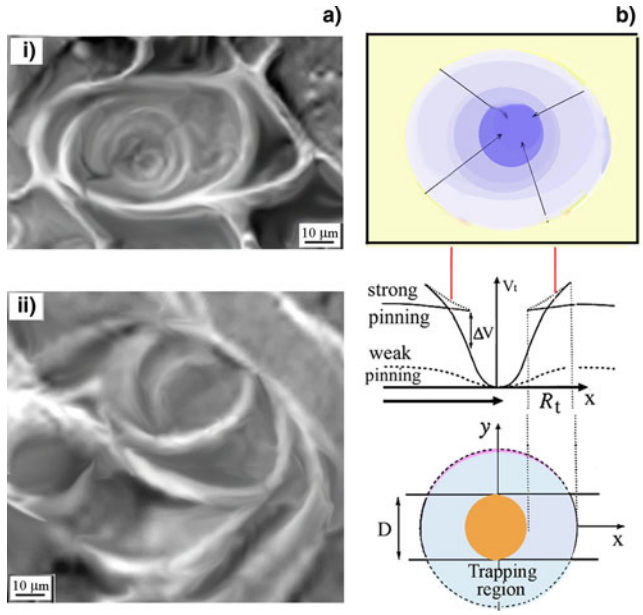

Fig. 11. Trapping of the filament-ribbon at the hole (assumed the "point defect") with the coiling SO. (a) SEM micrographs of the filament-ribbon trapped at the hole (cavity) which form the open-loop structure (i), and the multiple coils of closed-loop ribbons around two holes at few layers giving rise to the 3D coil SO (ii). (b) The elongated cavity with a hole (most similar to the real situation), representing a point defect surrounded by a liquid shell (trapping region) of radius R_t. Trapping of the filaments and ribbons is caused by the potential V_t. The trapping force $F_t = -\partial/\partial x$ (V_t), where $V_t = \Delta p$ and Δp is the pressure difference between the point defect and the surrounding area. The corresponding trapping potential V_t and the effect of the trapping force on the ribbon configuration as a kind of landscape is schematically shown in the lower picture diagram, where the trapping potential is shown circular (symmetric) for simplicity.

https://doi.org/10.1017/S026303461700009X Published online by Cambridge University Press

shape with diameter ~15–20 μm (or more), which is much larger than the core size of vortex filament (3–7 μm, usually). In close interaction with rigid spheres and holes (cavities-collapsed soft spheres or bubbles) – vortex filaments become trapped giving rise to complex configurations (Lugomer *et al*., 2007). The trapping results in the pinning of filament at the rigid sphere, which can be interpreted on the basis of the Pedrizzetti model (Pedrizzetti, 1992). More complex behavior such as looping and spiraling of filament around the sphere as the result of trapping, can be interpreted on the basis of the Shwarz model (Schwarz, 1985). The model describes vortex filament capture by a sphere or equivalently by a hemispherical protrusion, because around the point defect the boundary field exists, which tends to move the filament around the sphere (Schwarz, 1985). When the filament gets close enough, a cusp is pulled out by the boundary field of a sphere, causing the vortex to approach the sphere infinitely being finally pinned (Schwarz, 1985).

Pinning of filaments and ribbons (strings) on material defects is well known to occur in various physical, chemical, and biological systems. Generally speaking, the filaments *or the string-like structures* are pinned to the defects in various systems, an example of which is pinning of the magnetic flux strings in superconductors (Tonomura *et al.*, 2001; Blatter *et al.*, 2004), pinning of carbon nanotubes to defects on silicon substrate (Tsukruk *et al.*, 2004), pinning of spiral vortex filaments like various biological strings in excitable media (Pazo *et al*., 2004), etc. When completing the list with recently observed pinning of magnetic flux filaments in the Sun's penumbra (Thomas *et al*., 2002), one can say that pinning is a common phenomenon taking place in the filamentary organized matter from the atomic to the astrophysical scales.

Trapping of vortex ribbon at the cavity (the point defect) can be described by the trapping potential, V_t, originating from the pressure difference when the filament ribbon is in the close vicinity of a defect, either because of self-induction, or because of shear flow. The pressure difference or the hydrodynamic force is responsible for trapping at the distances $R \leq R_t$, where R_t is the trapping radius (Fig. 11b) (Lugomer *et al*., 2007). The topmost illustration in Figure 11b shows the point defect (elongated cavity with a hole) formed by the bubble collapse. Trapping of the filament ribbon by the trapping potential V_t is schematically shown in Figure 11b (middle). The trapping (drag) force is $F_t = -\partial/\partial x\ (V_t)$, where $V_t = \Delta p$, and Δp is is the pressure difference between the point defect and the surrounding area. The trapping potential, V_t, and the effect of the trapping force on the ribbon configuration is schematically shown in the lower picture diagram; the trapping potential is shown with circular symmetry for simplicity. The ribbon looping around a hole occurs via continuous bending similar to the spiraling of an elastic rod. The process is associated with the vortex-ribbon splitting because of the strong strain field surrounding a hole (Lugomer *et al*., 2007).

The high trapping potential of a cavity (hole) (Fig. 11) causes the formation of ribbon coils, of closed-loop structures as well as spiraling down cavity. It also causes the formation of closed loops with more or less complex knots, but the dense winding and merging with the nearby structures causes their configuration difficult to be resolved. Various fluid mechanic phenomena, like vortex filament bending, looping, and spiraling on point defects (spheres and cavities) have been studied in laser–matter (indium) interactions (Lugomer *et al*., 2007). Also, the other phenomena such as vortex filament reconnection, merging, and undulation (Lugomer *et al.*, 2007), as well as the formation of ribbons and ribbon helicoids, etc. (Lugomer & Fukumoto, 2010) have been studied in laser–matter interactions on various targets. In these interactions, it was naturally to assume viscous phenomena like other authors (Pedrizzetti, 1992), while some of them assume inviscid phenomena (Schwarz, 1985).

Generally speaking, interaction of filaments with (small) material defects is well known to occur in various physical, chemical, and biological systems. An example is the spiraling of waves and vortex filaments around defects in active media obtained as the solution of Ginsburg–Landau equation (Pazo *et al.,* 2004). Although the forces in these systems are different, the effects on the filaments with formation of complex structures as well as their topology are the same. Interestingly, similar behavior was also found in the steady configurations of a vortex filament embedded in a point-source or point-sink flow in three dimensions, which shows looping bending and spiraling quite similar to the interaction of filaments and point defects (Fukumoto, 1997).

Regarding the spiraling around sphere, it was assumed that the boundary field of point defect acts to distort the filament such as to generate a self-induced motion toward the sphere (defect). The frictional component of the motion also causes the filament to spiral in, and in fact becomes the main factor when the filament is far away. As the result, an initially straight filament will undergo an inward-spiraling motion (Schwarz, 1985).

For the analysis of dynamics, such spiraling and knotted filament ribbons can be assumed as the "…. closed solution curves of the vortex filament equation and the periodic problem connected with the nonlinear Schrödinger (NLS) equation…." (Calini & Ivey, 2001; Ivy, 2005). The knot types of finite gap solution are related with the corresponding NLS potential, but this is out of scope of this paper. For this aspect of the problem the reader is directed to the mathematical literature (Calini & Ivey, 2001; Ivy, 2005).

Figure 12 shows a 3D flow separation of incoming fluid into "A", "B", and "C" ribbon branches of which "B" and "C" are bended under ~90° with respect to the ribbon flow "A". The ribbon flow "A" makes an open loop around the cavity (collapsed bubble) in the backward direction schematically shown in the excerpt (upper right). The other excerpt (upper left), schematically shows the separation of the incoming flow into two branches (left and right) that form the open-loops around the cavities. The trapping potential V_t is not as strong as in the case in Figure 11 and only

https://doi.org/10.1017/S026303461700009X Published online by Cambridge University Press

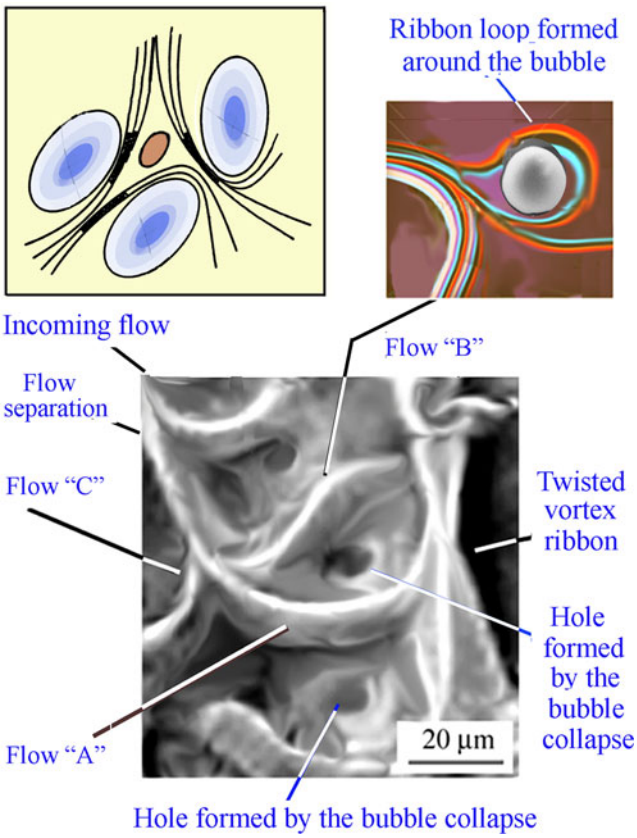

Fig. 12. SEM micrograph of vortex ribbon trapping by the trapping potential of the cavities with the hole. The trapping potential is not very strong, so that ribbons make only the open loop around the holes. The incoming flow is separated into three ribbon flow branches: flow A, flow B, and flow C. Every one of them enters close interaction with the hole inside the trapping distance radius, R_t. The flow separation and looping around the holes (cavities) as the point defects is schematically shown in the excerpt (upper left). The looping around the bubbles with the change of direction of the ribbon flow is schematically shown in the excerpt (upper right).

changes the direction of the ribbon flow. The ribbon "A" makes a loop around the cavity with the hole also formed by the bubble collapse (Lugomer, 2016*b*). The ribbon "B" is strongly bended around the bubble (hole) with tendency to form a loop. Generally, such trapping at the point defect (the spike or bubble) starts with approaching to the cavity (sphere); the vortex ribbon first aligns itself along the circumference in a straight form; then, closer to the cavity (sphere) it becomes arc bended. Finally, at very small distance the filament is turned backward and the arc-bended segment becomes a loop. (Lugomer *et al.*, 2007). It may be also merged with the nearby ribbon as seen at the right side of the micrograph. This ribbon (bypassing the hole) is exposed to the local forces, which cause twisting and the formation of knots (Lugomer & Fukumoto, 2010).

3.3.3.3. Interaction of flow stripes and ribbons with mushroom-shape spikes. Interaction of vortex filament-ribbons with two deformed RTI mushroom-shape spikes as well as merging of two mushroom spikes are shown in Figure 13. This figure clearly shows two mushroom spikes at small distance connected by a bridge what indicates merging. This effect is not a common occurrence in laser experiments, but appears in the experiments performed in the SCC. It was not observed in the whole region, but only in some domains. In such domains, all other structures in the base-plane are deformed or tangled. Since the merging of spikes does not normally appear (in contrast to bubble merging) this phenomenon seems to be the effect of most probably of the strong reshocks in such domains. An argument in favor is the similarity of this picture to Figure 9 (especially to Fig. 9a), and to the numerically simulated sequences of mushroom spikes, which approach each other under reshock (Fig. 8b) (Zhang *et al.*, 2006).

This figure also shows the filament-ribbons incoming from above which are layered one above the other and form 3D configuration. One of the ribbons is pinned at the mushroom spike (upper left) what can be interpreted on the basis of the Schwartz model for the filament pinning at protrusion (Schwarz, 1985; Lugomer *et al.*, 2007). The pinned ribbon makes the static irregular structure in the base of the spike (Fig. 13). It seems that there is a deformed ring around the RTI with a damped mushroom cap. The other ribbon (center) makes a large loop around the spike because its trapping potential is not strong enough to capture the ribbon. The vortex filament in Figure 13 (upper right) is splitted into two

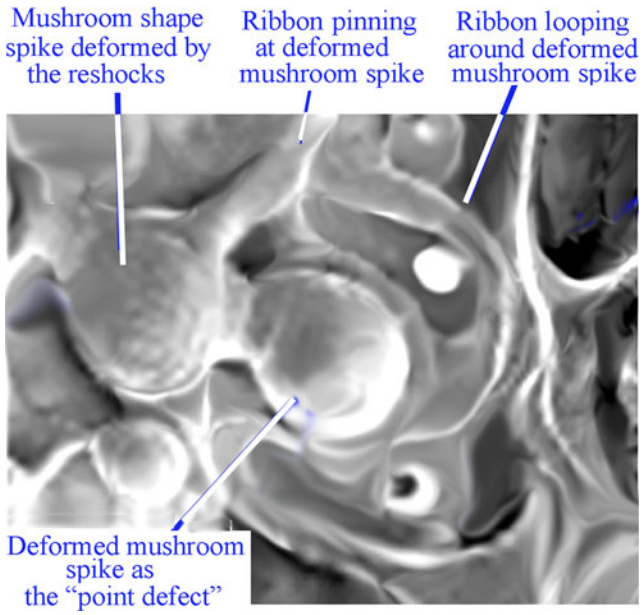

Fig. 13. SEM micrograph of vortex ribbon trapping at deformed mushroom-shape spike. A 3D flow separation of the incoming flow into few ribbons (upper, center) trapped by the trapping potential of the spikes. One ribbon branch is pinned at the spike, while the other two at the right side make loops around the spike. The trapping potential causes a large loop around the spike. The ribbon flow (upper right) is splitted into one smaller ribbon branch, which makes a loop to the right and turns backward, while the other ribbon extends along the other structures been deformed sinusoidally.

https://doi.org/10.1017/S026303461700009X Published online by Cambridge University Press

branches; one, which makes a loop backward around the cavity (dark), and another filament branch which spreads up into a wide ribbon that passes along the other structures being wavy-like deformed due to transversal oscillation. Obviously, the mixing is relatively higher than in the domains of the small reshock effects, but it is still the large-scale and not the small-scale turbulent mixing.

4. CONCLUSION

Dominant RMI/RTI morphology in the NCR make the "wall"-like structures connected into the irregular, quasi-periodic web (corresponding to deformed 2D lattice formed in the random flow field). At A ~(0.85–0.65) and $\boldsymbol{M}$ ~(0.60–0.70) $\boldsymbol{M}_{\max}$, the RMI is followed by the RTI. The RTI mushroom spikes appearing at the nodal points of the web with discrete organization indicate a strong horizontal fluid flow. Structures formed by the first shock are exposed to the series of fast reshocks in the time of ~200–300 μs after pulse termination because of the extended life-time of the vapor–plasma plume in the SCC. The series of fast reshocks affects the topological complexity of the mushroom spikes and bubbles and of the base-plane structures. The space-time variation of the reshock intensity and direction, causes formation of domains of the weak reshock effects and domains of the strong reshock effects on the RMI/RTI structures.

(i) Weak reshocks do not affect much the high-symmetry RTI damped, the spherical mushroom-shape spikes and the prolate ellipsoidal ones. Also, they do not affect much (or affect only slightly) the base-plane structures (the nonlinear cnoidal and the line soliton waves as well as the vortex filaments). These large-scale structures correspond to the low-mixing, which in the latter phase is not transformed into small-scale fully turbulent mixing. These local coherent structures (inside a random flow field) are organized into the rosette-like configuration or the polygonal web and represent the new paradigm of wave-vortex turbulent mixing in the domains of weak reshocks.

(ii) Strong reshocks dramatically affect the RTI spherical mushroom-shape spikes and cavities causing deformation and symmetry breakup. The pressure variation and the local pressure and velocity gradients in the base-plane cause 3D fluid flow separation into stripes and vortex ribbons (the fluid coherent structures) The vortex ribbon flow is directed between the spikes and bubbles which may be understood as a kind of surface "point defects". The trapping potential of the "point defects" affects the ribbon flow and causes the complex organizational phenomena: ribbon pinning at the spike, looping around the spike or around the cavity with the hole, as well as the ribbon coiling around the hole. They represent the new paradigm of the low-mixing structures in the domains of strong reshocks.

It may be said that both domains, those experiencing weak and the strong reshocks, show only a low (turbulent) mixing, although the mixing is somewhat higher than in the first ones. Without transition to the small-scale turbulent mixing structures, the low-mixing large-scale structures and their configurations represent the new mixing paradigm. Therefore, the RTI/RMI small-scale fully turbulent mixing with stochastic distribution of temperature, density and entropy usually observed in the open configuration does not take place in the SC configuration.

ACKNOWLEDGEMENTS

This work has been supported by the Croatian Science Foundation under the project: IP-2014-09-7046. I thank to Prof N.J. Zabusky, Department of Physics of Complex Systems, Weizmann Institute of Science, Rehovot, Israel, for his comments and suggestions emphasizing the wave-vortex paradigm in turbulent mixing in the laser experiments. I also thank to Professor S. I. Abarzhi, Carnegie Mellon University, USA, for inspiring comments and valuable suggestions. Finally, I would like to thank to the referee for the comments which improved the paper.

REFERENCES

Abarzhi, S.I. (2000). Regular and singularlate-timeasymptotes of potential motion of fluuid with afree boundary. *Phys. Fluids* **12**, 3112–3120.

Abarzhi, S.I. (2008). Review of nonlinear dynamics of the unstable fluid interface: Consrvation laws and group theory. *Phys. Scr.* **T132**, 014012 (1–18).

Abarzhi, S.I. (2010). Review of theoretical modelling approaches of Rayleigh-Taylor instabilities and turbulent mixing. *Phil. Trans. R. Soc. A* **368**, 1809–1828.Abarzhi, S.I. (2016). Private communication.

Alon, U., Ofer, D. & Shvarts, D. (1996). Scaling Laws of Nonlinear RT and RM Instabilities. *Proc. 5*th *Int.Workshop on Compressible Turbulent Mixing*, (Young, R., Glimm, J. and Boston, B., eds.) World Scientific. www.damtp.cam.ac.uk/iwpctm9/proceedings/.../Alon_Ofer_Shvarts.pdf

Anuchina, N.N., Volkov, V.I., Gordeychuk, V.A., Es'kov, N.S., Ilyutina, O.S. & Kozyrev, O.M. (2004). Numerical simulation of R-T and R-M instability using MAH-3 code. *J. Comput. Appl. Math*. **168**, 11–20.

Biondini, G. (2007). Line soliton interactions of the Kadomtsev–Petviashvili equation. *Phys. Rev. Lett*. **99**, 064103 (1–4).

Blatter, G., Geshkenbein, V.B. & Koopmann, J.A.G. (2004). Weak to strong pinning crossover. *Phys. Rev. Lett*. **92**, 067009–067013.

Calini, A.M. & Ivey, T. (2001). Knot types, Floquet spectra, and finite-gap solutions of the vortex filament equation. *Math. Comput. Simul*. **55**, 341–250.

Chapman, P.R. & Jacobs, J.W. (2006). Experiments on the 3D incompressible R–M instability. *Phys. Fluids* **18**, 074101 (1–12).

Cohen, R.H., Dennevik, W.P., Dimits, A.M., Eliason, D.E., Mirin, A.A., Zhou, Ye., Porter, D.H. & Woodward, P.R. (2002). Three-dimensional simulation of a RM instability with two-scale initial perturbation. *Phys. Fluids* **14**, 3692–3709.

Dimotakis, P.E. (2000). The mixing transition in turbulent flows. *J. Fluid Mech*. **409**, 69–98.

https://doi.org/10.1017/S026303461700009X Published online by Cambridge University Press

Fukumoto, Y. (1997). Stationary configurations of a vortex filament in background flows. *Proc. R. Soc. Lond.* A **453**, 1205–1232.

He, X., Zhang, R., Chen, S. & Doolen, G.D. (1999). On the three-dimensional R–T instability. *Phys. Fluids* **11**, 1143–1152.

Hua, J. & Lou, J. (2007). Numerical simulation of bubble rising in viscous liquid. *J. Comput. Phys*. **222**, 769–795.

Ivy, T. (2005). Geometry and topology of finite-gap vortex filaments, in Seventh Int. Conf. on Geometry, Integrability and Quantification, June (2005). Varna, Bulgaria. SOFTEX, Sofia, p. 1–16. Editors, I.M. Miladinov and M. De Leon.

Kartoon, D., Oron, D., Arazi, I. & Shvartz, D. (2003). Three-dimensional Rayleigh–Taylor and Richrmyer–Meskhow instabilities at all density ratios. *Laser Part. Beams* **21**, 327–334.

Khusnutdinova, K.R., Klein, C., Matveev, V.B. & Smirnov, A.O. (2013). On the elliptic cylindrical Kadomtsev–Petviashvili equation. *Chaos* **23**, 013126 (1–14).

Klein, C., Matveev, V.B. & Smirnov, A.O. (2007). Cylindrical Kadomtsev–Petviashvili equation: Old and new results. *Theor. Math. Phys*. **152**, 1132–1144.

Kodama, Y. (2004). Young diagram and N-soliton solutions of the KP equation. *J. Phys. A: Math. Gen*. **37**, 11169–11190.

Koochesfahani, M.M. & Dimotakis, P.E. (1986). Mixing and chemical reactions in a turbulent liquid mixing layer. *J. Fluid Mech*. **170**, 83–112.

Lazer, D. (1955). On the instability of superposed fluids in a gravitational filed. *Astrophys. J*. **122**, 1–12.

Long, C.C., Krivets, V.V., Greenough, J.A. & Jacobs, J.W. (2009). Shock tube 3D-experiments and numerical simulation of the single-mode, 3D RM instability. *Phys. Fluids* **21**, 114104 (1–9).

Lugomer, S. (2016*a*). Laser-matter interactions: Inhomogeneous Richtmyer–Meshkov and Rayleigh–Taylor instabilities. *Laser Part. Beams* **34**, 123–135.

Lugomer, S. (2016*b*). Laser generated Richtmyer–Meshkov and Rayleigh–Taylor instabilities and nonlinear wave paradigm in turbulent mixing. I. Central region of Gaussian spot. *Laser Part. Beams* **34**, 687–704.

Lugomer, S. & Fukumoto, Y. (2010). Generation of ribbons, helikoids, and complex Scherk surfacesin laser–matter interactions. *Phys. Rev. E* **81**, 036311 (1–11).

Lugomer, S., Fukumoto, Y., Farkas, B., Szorenyi, T. & Toth, A. (2007). Supercomplex wave-vortex multiscale phenomena induced in laser–matter interactions. *Phys. Rev. E* **76**, 1–15.

Lugomer, S., Maksimovic, A., Geretovszky, Z. & Szorenyi, T. (2013). Nonlinear waves generated on liquid silicon layer by femtosecond laser pulses. *Appl. Surf. Sci*. **28**, 588–600.

Miles, A.R., Blue, B., Edwards, M.J., Greenough, J.A., Hansen, F., Robey, H., Drake, R.P., Kuranz, C. & Leibrandt, R. (2005). Transition to turbulence and effect of initial conditions on 3D compressible mixing in planar blast-wave-driven systems. *Phys. Plasmas* **12**, 056317 (1–10).

Oikawa, M. & Tsuji, H. (2006). Oblique interactions of weakly nonlinear long waves in dispersive systems. *Fluid Dyn. Res*. **38**, 868–898.

Pandian, A., Stellingwerf, R.E. & Abarzhi, S.I. (2016). Effect of wave interference on nonlinear dynamics of Richtmyer–Meshkov flows. *Phys. Fluids* accepted.

Pedrizzetti, G. (1992). Close interaction between a vortex filament and a rigid sphere. *J. Fluid Mech*. **245**, 701–722.

Pazo, D., Kramer, L., Pumir, A., Kanani, S., Efimov, I. & Krinsky, V. (2004). Pinning force in active media. *Phys. Rev. Lett*. **93**, 168303–168307.

Schwarz, K.W. (1985). Three-dimensional vortex dynamics in superfluid He4: Line-line and line-boundary interactions. *Phys. Rev. B* **31**, 5782.

Shu, S. & Yang, N. (2013). Direct numerical simulation of bubble dynamics using phase-field model and lattice Boltzmann method. *Ind. Eng. Chem. Res*. **52**, 11391–11403.

Sin'kova, O.G., Statsenko, V.P. & Yanilkin, Yu. (2007). Numerical Study of the turbulent mixing development of the air-SF6 interface at the shock-wave propagation with large Mach numbers. (in Russian). *VANT, Ser. TPF* **2/3**, 3–17.

Statsenko, V.P., Yanilkin, Yu. & Zmaylo, V.A. (2014). Direct numerical simulation of turbulent mixing. *Philos. Trans. R. Soc. A* **371**, 20120216 (1–19).

Stellingwerf, R., Pandian, A. & Abarzhi, S.I. (2016*a*). Wave interference in Richtmyer–Meshkov flows, *69th Annual Meeting of the APS Division of Fluid Dynamics*, November 20–22, 2016; Portland, Oregon, vol. **61**, http://meetings.aps.org/Meeting/DFD16/Session/R18.6

Stellingwerf, R., Pandian, A. & Abarzhi, S.I. (2016*b*). Wave interference in Richtmyer–Meshkov flows, *58th Annual Meeting of the APS Division of Fluid Dynamics, October 31–November 4 2016*; San Jose, California, vol. **61**, http://meetings.aps.org/Meeting/DPP16/Session/YP10.52

Suponitsky, V., Barsky, S. & Froese, A. (2014). On the collapse of a gas cavity by an imploding molten lead shell and Richtmyer-Meshkov instability. *Comput. Fluids* **89**, 1–19.

Suponitsky, V., Froese, A. & Barsky, S. (2013). A parametric study examining the effects of re-shock in RMI. *Soft Condensed Matter* **2013**, 1–43. Arxiv. Web. 17 May 2014.

Thomas, J.H., Weissl, N.O., Tobias, S.M. & Brummel, N.H. (2002). Downward pumping of magnetic flux as the cause of filamentary structures in sunspot penumbrae. *Nature*, London, **420**, 390–393.

Tonomura, A., Kasai, H., Kamimura, O., Matsuda, T., Harada, K., Nayakama, Y., Shimoyama, J., Kishio, K., Hanaguri, T., Kitazawa, K., Sasase, M. & Okayasu, S. (2001). Observation of individual vortices along columnar defects in high temperature superconductors. *Nature*, London, **412**, 620–622.

Tsukruk, V.V., Ko, H. & Peleshanko, S. (2004). Nanotube surface arrays: Weaving, bending, and assembling on patterned silicon. *Phys. Rev. Lett*. **92**, 065502–065506.

Unverdi, S.O. & Trygvason, G. (1992). A front-tracking method for viscous, incmpressible multi-fluid flows. *J. Comput. Phys*. **100**, 25–37.

Zabusky, N.J., Lugomer, S. & Zhang, S. (2005). Micro-fluid dynamics via laser metal surface interactions: Wave-vortex interpretation of emerging multiscale coherent structures. *Fluid Dyn. Res*. **36**, 291.

Zhang, Q. (1998). Analytical solutions of Lazer-type approach to unstable interfacial fluid mixing. *Phys. Rev. Lett*. **81**, 3391–3394.

Zhang, Y.-T., Shu, C-W. & Zhou, Ye. (2006). Effects of shock waves on R–T instability. *Phys. Plasmas* **13**, 062705 (1–13).

Zhou, Ye., Remington, B.A., Robey, H.F., Cook, A.W., Glendinning, S.G., Dimits, A., Buckingham, A.C., Zimmerman, G.B., Burke, E.W., Peyser, T.A., Cabot, W. & Eliason, D. (2003). Progress in understanding turbulent mixing induced by RT and RM instabilities. *Phys. Plasmas* **10**, 1883–1896.

Youngs, D.I. (2013). The density ratio dependence of self-similar Rayleigh–Taylor mixing. *Philos. Trans. R. Soc.* A **371**, 20120173 (1–15).

https://doi.org/10.1017/S026303461700009X Published online by Cambridge University Press